Earth and Planetary Science Letters 576 (2021) 117213

Contents lists available at ScienceDirect

Earth and Planetary Science Letters

www.elsevier.com/locate/epsl

Density and viscosity changes between depleted and primordial mantle at ∼1000 km depth influence plume upwelling behavior

Guanjie Xiang [a], Zhensheng Wang [a,*], Timothy M. Kusky [a,b]

[a] State Key Lab of Geological Processes and Mineral Resources, Center for Global Tectonics, School of Earth Sciences, China University of Geosciences, Wuhan, China
[b] Three Gorges Research Center for Geohazards, China University of Geosciences, Wuhan, China

ARTICLE INFO

Article history:
Received 9 March 2021
Received in revised form 9 September 2021
Accepted 13 September 2021
Available online xxxx
Editor: J. Badro

Keywords:
1000-km discontinuity
mantle plume
depleted mantle
mantle stratification
plume ponding
primordial mantle

ABSTRACT

Earth's mantle is more than 2800 km deep, compositionally heterogenous, and potentially stratified. However, understanding of its heterogeneities and stratification is limited. Recently, plume-like anomalies were detected to exhibit different types of anomalous behavior at ∼1000 km depth, where they laterally pond, neck or broadly penetrate to the upper mantle, suggesting that their behavior may be influenced by possible viscosity or density stratification near this depth. However, the specific key reasons are unclear. Here, we use 2D thermal-mechanical-chemical modeling to constrain the key factors causing these large-scale plume-related anomalies. Upward mantle plume penetration at ∼1000 km depth is mainly caused by large source volume and excess temperature, whereas its necking and lateral extension at this depth can only be caused by viscosity and composition-related density stratification, respectively. Considering the various plume behaviors at this proposed boundary, we show that Earth's mantle is likely heterogeneously stratified at ∼1000 km depth, with regional viscosity and/or density changes of different lateral scales and vertical gradients. We speculate that this boundary separates the upper depleted mantle from the primordial mantle domain below. This fundamental boundary has been progressively evolving during stratification of Earth's mantle through melt extraction and mantle stirring throughout Earth history.

1. Introduction

It has been proposed that Earth's interior has a fundamental discontinuity at mid-mantle depths of ∼400-1000 km, marking the mantle transition zone (MTZ) between mantle layers below and above (e.g., Bullen, 1940, 1947). The lower boundary of the MTZ was later reclassified as the 660 km phase boundary according to seismic and petrophysical studies (Ito and Takahashi, 1989; Ringwood, 1970; Wood, 1990), but the mystery of ∼1000 km discontinuity persists. Recently, more and more seismic observations (Durand et al., 2017; French and Romanowicz, 2015; Fukao and Obayashi, 2013; Moulik and Ekström, 2014; e.g., Ritsema et al., 2011) suggest that a series of subducted slabs (e.g., Peru, Java, Tonga-Kermadec, Central America, northern Kuriles) (Fukao and Obayashi, 2013) tend to penetrate or stagnate at ∼1000 km depth whereas plumes/upwellings (e.g., Pitcairn, Cape Verde, Hawaii, Canary) tend to penetrate (Fig. 1a, b), neck (Fig. 1c, d) or pond (Fig. 1e, f) at this depth (French and Romanowicz, 2015). The narrow plume conduits during necking may be invisible because of limitations of seismic resolution, but can be deduced from their shallower and deeper counterparts (French and Romanowicz, 2015), although this kind of deduction is sometimes inaccurate. Researchers (e.g., Durand et al., 2017; Waszek et al., 2018) speculate that the different behaviors of slabs and plumes at ∼1000 km depth may be influenced by mineral phase transitions, viscosity stratification (gradual increase of viscosity from 660 km to 1000 km depth) (Čížková and Bina, 2019; Rudolph et al., 2015), or changes in chemical composition, but the specific cause is uncertain.

Under temperature and pressure conditions appropriate for 1000 km depth of Earth's mantle, no mineral phase transitions can explain the anomalies mentioned above (e.g., Durand et al., 2017; Waszek et al., 2018). Recently, geodynamic numerical modelers have proposed that a change in chemical composition and its related density jump with depth can lead to slab penetration and stagnation at ∼1000 km depth (Ballmer et al., 2015). Later works demonstrated that a viscosity reduction between 660 and 1200 km depths can also lead to long-term slab deflection and penetration at ∼1000 km (Čížková and Bina, 2019). However, the relative importance and distribution of the density or viscosity stratification is only partly addressed via these slab subduction models.

* Corresponding author.
E-mail address: jasonwang@cug.edu.cn (Z. Wang).

https://doi.org/10.1016/j.epsl.2021.117213

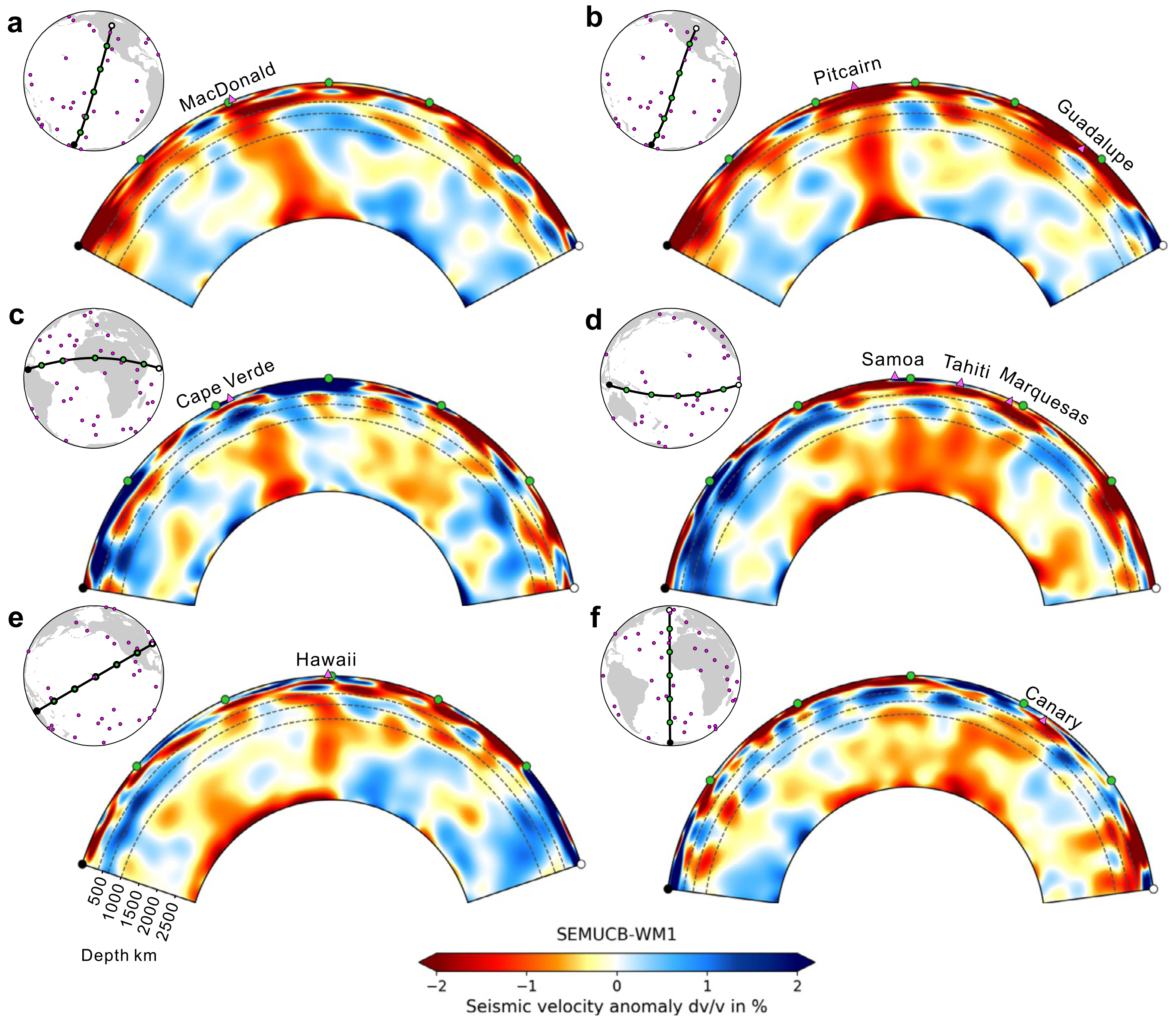

Fig. 1. Seismic tomographic profiles below some hot spots (French and Romanowicz, 2015). (a-b) Broad plume upwelling and penetration (e.g., MacDonald, Pitcairn) at ∼1000 km depth. (c-d) Plume necking (e.g., Cape Verde, Tahiti) at ∼1000 km depth. (e-f) Plume lateral ponding (e.g., Hawaii, Canary) at ∼1000 km depth. The 410, 660 and 1000 km depth are shown on the profiles (dashed dark lines). The maps in the upper left corner of each subfigures show the intersection of the cross-section with the surface. The dark and white circles indicate the direction of the cross-section.

We suggest a new innovative test to solve this question, which is embedded in characterizing various behaviors of deep, upward-protruding plumes mentioned above (Fig. 1) at similar depths as the ∼1000 km slab stagnation. However, whether the penetrating, necking and ponding of plumes at ∼1000 km depth is caused by viscosity or density stratification, remains unanswered.

In this work, we use numerical simulations to analyze the influences of viscosity and compositional density layering on the dynamics of deep plumes at ∼1000 km depth. We designed different groups of 2D models with different mantle viscosities or density structures, considering viscosity and compositional density changes at ∼1000 km depth. In each group, we designed models with different source sizes (initial volume of the source region) and excess temperatures. This allows us to investigate the dynamics of different mantle plumes at ∼1000 km depth, including broad penetration, necking, ponding, foundering and aborting.

2. Methods

The geodynamic modeling framework Underworld (Moresi et al., 2003) is used to set up numerical models and to track the changes of different material properties via Lagrangian particles embedded within Euler elements. An extended Boussinesq approximation is adopted, regarding the mantle as an incompressible fluid medium. Then the conservation equations of mass (1), momentum (2) and energy (3) are solved to model plume evolution.

$$\nabla \cdot u = 0 \tag{1}$$

$$\nabla \cdot \left[\eta \left(\nabla_u + \nabla_u\right)^{\mathrm{T}}\right)\right] - \nabla \mathrm{P} = -\rho g \tag{2}$$

$$\rho \mathrm{C_p}\left(\frac{\partial \mathrm{T}}{\partial \mathrm{t}} + u\nabla \mathrm{T}\right) - \nabla\left(\kappa \nabla \mathrm{T}\right) = -\alpha\rho v_z \mathrm{T} \tag{3}$$

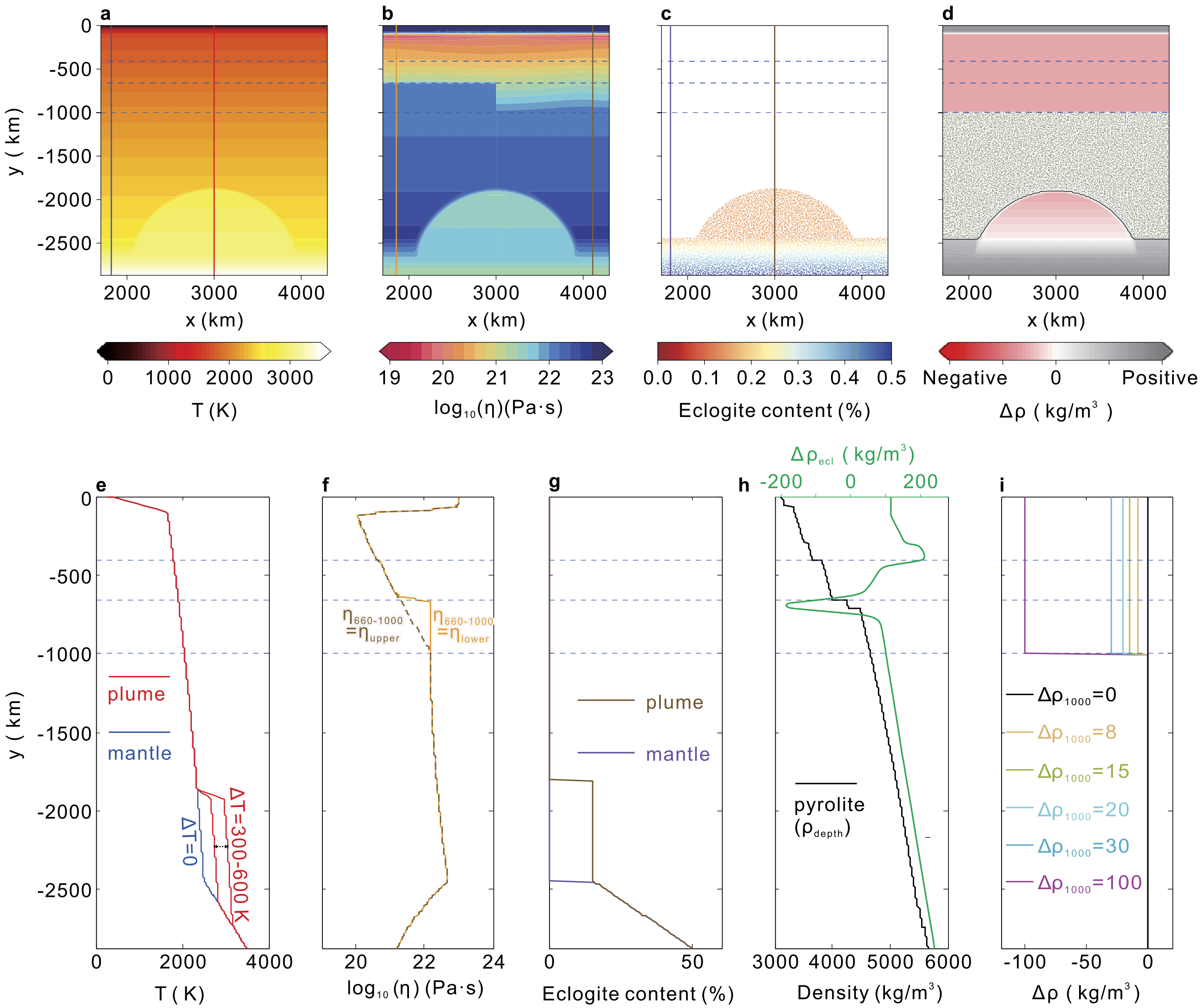

Fig. 2. Model initial conditions. Dashed blue lines mark the depth lines 410, 660 and 1000 km, respectively. Model domain is 2870 km deep and 6000 km wide, and only the middle part near the plume axis is shown. The radius of the plume source region is changed in different models from 600-1400 km, corresponding to initial volume of 0-0.88$\times 10^9$ km^3. (a) Temperature field, the excess temperature (ΔT) is changed in different models, ranging from 300-600 K. (b) Viscosity field of different model groups. (left half shows groups without viscosity stratification at ~1000 km, right half is another group with viscosity stratification at ~1000 km). (c) Eclogite content. (d) Density differences between model rocks (an example) and pyrolite, influenced by eclogite content, temperature and density contrast at ~1000 km. Green particles indicate primordial materials. (e) Temperature profiles of mantle and plume in Fig. 2a. (f) Viscosity profiles of different model groups in Fig. 2b. (g) Eclogite content profiles of mantle and plume in Fig. 2c. (h) Density profile of pyrolite and density difference between eclogite and pyrolite according to experimental data (Dannberg and Sobolev, 2015; Yan et al., 2020). (i) Density contrast at ~1000-km-depth used in different model groups. The curves with different colors indicate the $\Delta\rho_{1000} = 0$, 8, 15, 20, 30 and 100 kg/m^3, respectively. (For interpretation of the colors in the figure(s), the reader is referred to the web version of this article.)

where, u is velocity, P is pressure, T is temperature, η is viscosity, ρ is density, g is gravitational acceleration, C_p is the specific heat, t is time, κ the coefficient of thermal conductivity, α the coefficient of thermal expansion, and v_z the vertical component of velocity.

The model domain is 2870 km deep and 6000 km wide, which is discretized into 300 $\times$ 140 elements, with 30 Lagrangian particles in each element (Fig. 2a). The temperature field of the ambient mantle (blue profile in Fig. 2e) follows the adiabatic profile given by Katsura et al. (2010), with a thermal boundary layer of linear temperature increase of ~1000 K near the bottom wall (Dannberg and Sobolev, 2015; Farnetani, 1997). To test the influences of different plumes, a hot source region (semicircle) with different size (hereby initial volume) and excess temperature ΔT (relative to the ambient mantle) is set above the bottom boundary of the model domain for different model groups (Fig. 2). The size and ΔT change from 0-0.88$\times 10^9$ km^3 and 300-600 K, respectively, in different models for each groups, covering a large range of possible volume and excess temperature for the plume source region constrained by geophysical and geological studies (Farnetani, 1997; Sobolev et al., 2011; Zhong, 2006). The plume generation zone near core-mantle boundary is rich in dense materials, such as eclogite or other Fe-rich rocks (Dannberg and Sobolev, 2015; Farnetani, 1997). A high eclogite concentration as supported by numerical models (Dannberg and Sobolev, 2015) and geologic observations (Sobolev et al., 2011) is considered for the deep plume source region, including the thermal boundary layer (with 15-50% eclogite) and the semicircle region (with $\geq$15% eclogite) (Dannberg and Sobolev, 2015) (Fig. 2c).

The rock density can be described as a function of temperature (P) and pressure (T) and as shown below:

$$\rho = \rho_{depth}\,(1 - \alpha \Delta T) - \Delta\rho_{1000} + c_{ecl}\Delta\rho_{ecl} \tag{4}$$

ρ_{depth} is the reference density of mantle pyrolite, as a function of depth, considering major phase changes in the mantle (Xu et al., 2008; Yan et al., 2020). ΔT is the temperature difference related to the mantle adiabatic profile. α is the coefficient of thermal expansion changing with temperature and pressure (Tosi et al., 2013). The model is simplified to be homogenously layered at ∼1000 km depth, consistent with other numerical model setups (Ballmer et al., 2015; Čížková and Bina, 2019) to investigate the influences of different layering processes. The $\Delta\rho_{1000}$ is the compositional density jump at ∼1000 km depth, tracked by properties on particles. The value of $\Delta\rho_{1000}$ ranges from 0-100 kg/m^3, covering a large value range described and investigated by previous studies (Ballmer et al., 2017; Gülcher et al., 2020a,b). $\Delta\rho_{\text{ecl}}$ is the density difference of eclogite related to the reference density, and c_{ecl} is the eclogite content.

The coefficient of thermal expansion (α) and thermal conduction (κ) are simplified as functions of temperature (T) and pressure (P) (Tosi et al., 2013) shown below:

$$\alpha\,(T,P) = \left(a_0 + a_1 T + a_2 T^{-2}\right) exp\,(-a_3 P) \tag{5}$$

$$\kappa\,(T,P) = (c_0 + c_1 P)\left(\frac{300}{T}\right)^{c_2} \tag{6}$$

where a_0, a_1, a_2, a_3, c_0, c_1, c_2 are changed between different phases and given in Table S1 in Supplementary Information 1.

We use a composite rheology to define the viscosity (η_{upper}) of the upper mantle (van den Berg et al., 1993), which includes diffusion creep (η_{diff}), dislocation creep (η_{disl}), and a stress limiter (η_y) (van Hunen et al., 2002) as shown below:

$$\eta_{upper} = \left(\frac{1}{\eta_{diff}} + \frac{1}{\eta_{disl}} + \frac{1}{\eta_y}\right)^{-1} \tag{7}$$

The diffusion creep η_{diff} can be described as a function of pressure (P) and temperature (T) (Čížková et al., 2012; van Hunen et al., 2002) and as shown below:

$$\eta_{diff} = \frac{1}{A_{diff}} exp\left(\frac{E_{diff} + PV_{diff}}{RT}\right) \tag{8}$$

The dislocation creep (η_{disl}) can be described as a function of pressure (P), temperature (T) and second invariant of the strain rate tensor ($\dot{\varepsilon}_{II}$) (Čížková et al., 2012; van Hunen et al., 2002) as shown below:

$$\eta_{disl} = \frac{1}{A_{disl}^{\frac{1}{n}}}\dot{\varepsilon}_{II}^{(1-n)/n} exp\left(\frac{E_{disl} + PV_{disl}}{nRT}\right) \tag{9}$$

After (van Hunen et al., 2002), a stress limiter η_y can be described as a function of second invariant of the strain rate tensor ($\dot{\varepsilon}_{II}$):

$$\eta_y = \tau_y \dot{\varepsilon}_y^{-1/n_y} \dot{\varepsilon}_{II}^{1/n_y - 1} \tag{10}$$

For the mantle rheology below 1000 km depth, the viscosity (η_{lower}) is equivalent to the viscosity of diffusion creep (η_{diff}):

$$\eta_{lower} = \eta_{diff} \tag{11}$$

To investigate the effect of the viscosity stratification on the evolution of the deep plume at ∼1000 km depth, a layer between 660-1000 km depths is designed to follow the rheological law of the upper mantle or lower mantle, respectively (Čížková and Bina, 2019):

$$\eta_{660-1000} = \begin{cases} \eta_{upper} & \text{with 1000 km jump} \\ \eta_{lower} & \text{no jump} \end{cases} \tag{12}$$

Through changing the density structure and viscosity structure of the lower mantle, here by means of $\Delta\rho_{1000}$ and $\eta_{660-1000}$, we designed 7 groups of models, including 203 models to investigate the evolution process of a deep plume at ∼1000 km depth. In each group, the volume and excess temperature (ΔT) of the thermal anomaly region vary from 0-0.88×10^9 km^3, and 300-600 K, respectively, covering large ranges comparable with the observations mentioned above. More details on the model setup are presented in Table S2 in Supplementary Information 1.

3. Results

3.1. Main types of model evolution at ∼1000 km depth

According to the behavior of the deep plume at ∼1000 km depth, the 203 models (Supplementary Information 2) for all groups can be classified into 5 types (Fig. 3). In Type I, thermal anomalies can not upwell to ∼1000 km depth, so we name them "aborting type" (Fig. 3a). In Type II, upwelling can reach the 1000 km depth, but is laterally developed at ∼1000 km depth to form plume lateral ponding effects, and without further upwelling or eruption, we thus call them "ponding type" (Fig. 3b). In Type III, the deep plume can pass through the 1000 km depth with a broad conduit until it enters the low-viscosity upper mantle and becomes narrow, and is thus called "broad penetration type" (Fig. 3c). In Type IV, the deep plume can pass through the 1000 km depth, but its conduit becomes dramatically narrow above this depth (Fig. 3d), we call this "necking type". Type V is a subtype or the next stage of Type III, because after the cooling of the plume materials by ambient mantle or plates, their thermal buoyancy is counteracted and surpassed by their compositionally negative buoyancy. These materials are then foundered back again to ∼1000 km depth or deeper (Fig. 3e). We named this type as "foundering type". Thus, this foundering type has features of broad penetration, which is followed by foundering (Fig. 3e). In fact, foundering is the final fate of all the compositionally dense plumes. However, the foundering stage of the necking type modeled here does not show any laterally extending effects at ∼1000 km depth, whereas the foundering materials of aborting and ponding types should be below ∼1000 km depths and thus are not further described here.

These types of model evolution are mainly controlled by density or viscosity stratification at ∼1000 km depth according to our model results, and are also influenced by the initial volume and excess temperature of plumes as shown below (Fig. 4). Most of these parameters take effect essentially through the average value of the non-dimensional buoyancy ratio for the plume head region at specific depths (B_{depth}) (Davaille, 1999; Hansen and Yuen, 1988):

$$B_{depth} = mean\left(\frac{\Delta\rho_C}{\rho_{depth}\alpha\Delta T}\right) \tag{13}$$

$$\Delta\rho_C = \begin{cases} c_{ecl}\Delta\rho_{ecl} & \text{plume vs. the primodial layer} \\ c_{ecl}\Delta\rho_{ecl} + \Delta\rho_{1000} & \text{plume vs. the depleted layer} \end{cases} \tag{14}$$

where $\Delta\rho_C$ is the compositional density contrast, $\rho_{\text{depth}}\alpha\Delta T$ is the thermal density contrast (thermal buoyancy). When the ρ_{depth}, α or ΔT, described in the methods, are relatively small, thermal buoyancy can generally not counteract the negative buoyancy of the eclogitic component (buoyancy ratio >1 or close to 1 at the initial time then changed to be >1 during model evolution), and thus the aborting type was generated. However, when the buoyancy ratio is small enough (≪1) from the top of the source region to upper mantle depths, upwelling can smoothly pass through the

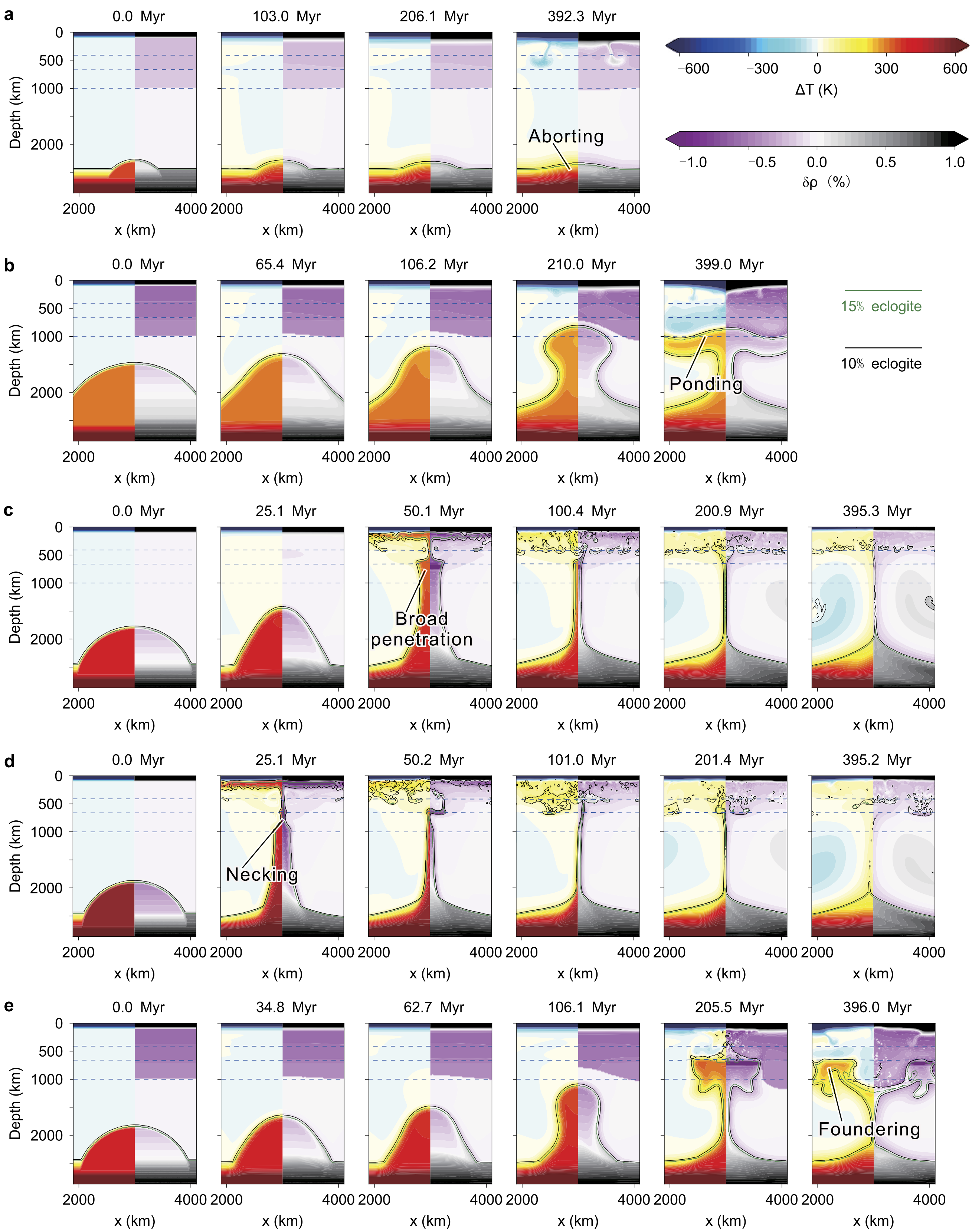

Fig. 3. The snapshots show four representative examples for the four types of model evolution, respectively. (a) Example of aborting type, in which ΔT = 350 K, initial volume= 0 km^3, $\Delta\rho_{1000} = 8$ kg/m^3 and $\eta_{660-1000}$ is equivalent to η_{lower}. (b) Example of ponding type (399.0 Myr), in which $\Delta T = 300$ K, initial volume= 0.80×10^9 km^3, $\Delta\rho_{1000} = 20$ kg/m^3 and $\eta_{660-1000}$ is equivalent to η_{lower}. (c) Example of broad penetration (50.1 Myr) type, in which ΔT = 400 K, initial volume= 0.88×10^9 km^3, $\Delta\rho_{1000} = 0$ kg/m^3 and $\eta_{660-1000}$ is equivalent to η_{lower}. (d) Example of necking type (25.1 Myr), in which ΔT = 550 K, initial volume=0.82×10^9 km^3, $\Delta\rho_{1000} = 0$ kg/m^3 and $\eta_{660-1000}$ is equivalent to η_{upper}. (e) Example of foundering type (396.0 Myr), in which ΔT = 400 K, initial volume= 0.71×10^9 km^3, $\Delta\rho_{1000} = 20$ kg/m^3 and $\eta_{660-1000}$ is equivalent to η_{lower}. The time and scale of ponding, foundering and necking are changes between models.

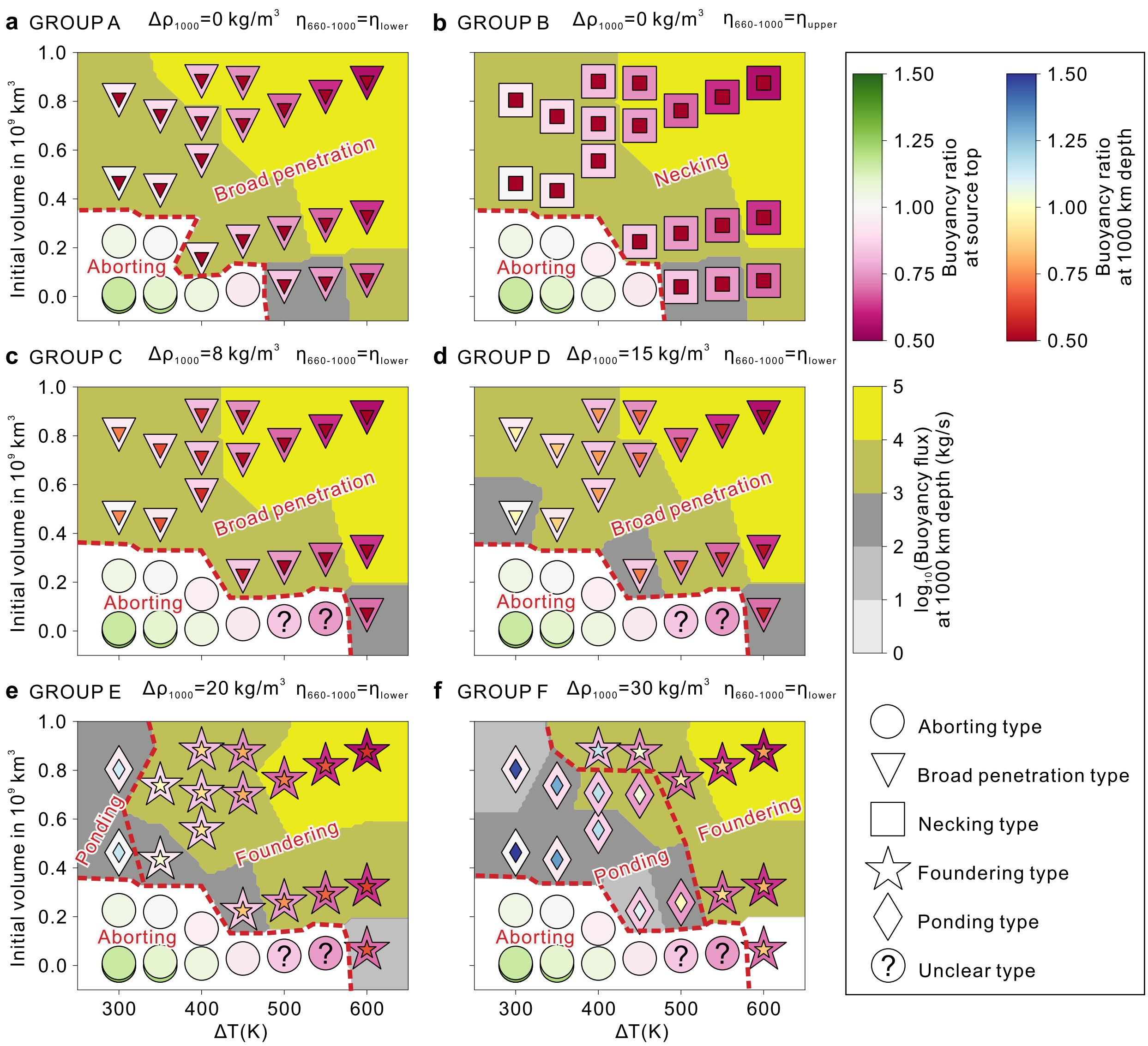

Fig. 4. Deep plume types in different model groups with changing excess temperature (ΔT) and initial volume of the source region. Colors of the larger markers denote average buoyancy ratio at the top of the source region at the initial time. Colors of the smaller markers denote average buoyancy ratio of the plume head as it reach the ~1000 km depth. Background contour field with colors denotes maximum buoyancy flux (MBF) at ~1000 km depth during ~400 Myr of model evolution. Dashed red lines indicate the possible boundaries of the plume types. (a) GROUP A, no density or viscosity stratification at ~1000 km depth, $\Delta\rho_{1000} = 0$, $\eta_{660-1000} = \eta_{\text{lower}}$, only aborting type and broad penetration type are formed. (b) GROUP B, no density stratification but with viscosity stratification at ~1000 km depth, $\Delta\rho_{1000} = 0$, $\eta_{660-1000} = \eta_{\text{upper}}$, only aborting type and necking type are formed. (c) GROUP C, $\Delta\rho_{1000} = 8$ kg/m^3, $\eta_{660-1000} = \eta_{\text{lower}}$, only aborting type and broad penetration type are formed. (d) GROUP D, $\Delta\rho_{1000} = 15$ kg/m^3, $\eta_{660-1000} = \eta_{\text{lower}}$, only aborting type and broad penetration type are formed. (e) GROUP E, $\Delta\rho_{1000} = 20$ kg/m^3, $\eta_{660-1000} = \eta_{\text{lower}}$, only aborting type, foundering and ponding type are formed. (f) GROUP F, $\Delta\rho_{1000} = 30$ kg/m^3, $\eta_{660-1000} = \eta_{\text{lower}}$, only aborting type, foundering and ponding type are formed. Unclear type is because of run time limitation (~400 Myr), during which the plume has still not been formed. More details of these 203 models are presented in Supplementary Information 2.

1000 km depth with a broad/necking shape, and form broad/necking plume pathways (Fig. 4). When the buoyancy ratio is smaller than 1 in the lower part of the lower mantle but finally becomes larger than 1 at ~1000 km depth, the plume ponds at ~1000 km depth.

The temporal effect of the buoyancy ratio can be parameterized by the maximum buoyancy flux (MBF) at ~1000 km depth through the evolution time of the mantle plume:

$$MBF = \max\left(\int_{r=0}^{r=r_{conduit}} 2\Delta\rho\,(r)\, v_z\,(r)\,\pi r dr\right) \tag{15}$$

where $\Delta\rho$ is the density difference between the plume and ambient mantle, including thermal and compositional effects, r the radial direction, r_{conduit} the radius of plume conduit, and v_z the vertical component of velocity. The value of MBF is taken at the peak time of the plume head stage. MBF=0 usually corresponds to aborting type plumes or plumes that have not risen to ~1000 km depth after ~400 Myrs of evolution (Fig. 4). Broadly penetrating, necking, and foundering types with upper-mantle penetration, mostly have larger MBF values ranging from 10^{2-5} kg/s (Fig. 4), which are comparable with plume flux catalogues and peak value ranges of previous plumes (Hoggard et al., 2020; Sleep, 1990). However, the ponding type mostly has a minor to moderate MBF value range (10^{1-4} kg/s) at ~1000 km depth (Fig. 4), indicating plume upwelling is restricted by the density barrier at this depth, especially when we compare different model groups as below.

3.2. GROUP A: no density or viscosity stratification at ∼1000 km depth

GROUP A is a reference group and is assigned no density or viscosity stratification near 1000 km depth, hence $\Delta\rho_{1000} = 0$ and $\eta_{660-1000} = \eta_{\mathrm{lower}}$. In GROUP A, only aborting and broad penetration types are obtained (Fig. 4a). When the average buoyancy ratio at the top of the source region is >1 or is becoming to >1, aborting types form, which leads to MBF values close to 0 at ∼1000 km depth. When the average buoyancy ratio is <1 from the top of the source region to depths shallower than 1000 km, broad penetration types with large MBF values may form.

3.3. GROUP B: with only viscosity stratification at ∼1000 km depth

GROUP B is used to test the influences of a viscosity change at ∼1000 km depth, hence $\Delta\rho_{1000} = 0$ and $\eta_{660-1000} = \eta_{\mathrm{upper}}$. In this group, the boundary of the aborting type is similar to that in the GROUP A, whereas the broad penetration type in GROUP A are mostly replaced by the necking type in GROUP B (Fig. 4b) and no other types are produced. This means the viscosity stratification at ∼1000 km depth can only lead to plume necking at ∼1000 km depth, but can not lead to lateral ponding of plume materials there. The physics controlling aborting and passing is similar to that in GROUP A, yet the physics controlling necking is distinct and described in the discussion below.

3.4. GROUP C-D: with minor density contrast at ∼1000 km depth

GROUP C-F test the influences of density stratification near 1000 km depth, whereas C-D has very minor density contrast (8-15 kg/m^3). The $\Delta\rho_C$ in Eq. (13) at ∼1000 km depth thus becomes to $c_{\mathrm{ecl}}\Delta\rho_{\mathrm{ecl}} + \Delta\rho_{1000}$ (Eq. (14)). In GROUP C, $\Delta\rho_{1000} = 8$ kg/m^3 and $\eta_{660-1000} = \eta_{\mathrm{lower}}$. In GROUP D, $\Delta\rho_{1000} = 15$ kg/m^3 and $\eta_{660-1000} = \eta_{\mathrm{lower}}$. These two groups are very similar to GROUP A, and only aborting and broad penetration types are obtained (Fig. 4c, d). The boundary between the aborting and broad penetration types are also similar to the one in GROUP A, just some models with broad penetration change to aborting types likely because of the limitation of running time. Our results show that minor density contrast can only lead to a slight increase of the buoyancy ratio at ∼1000 km depth, which can not restrict the plumes broad penetration there, for cases with large MBF values.

3.5. GROUP E-F: with moderate density contrast at ∼1000 km depth

In GROUP E-F, the mantle materials above 1000 km become more buoyant ($\Delta\rho_{1000} = 20 - 30$ kg/m^3), which restrains the plume buoyancy relative to the ambient mantle and hence enlarges the buoyancy ratio at ∼1000 km depth. It thus restricts the upwelling of the plume materials, and even promotes the foundering possibilities of compositionally-dense plume materials. Therefore, the foundering and ponding type emerge in these groups. With the increase of $\Delta\rho_{1000}$ from 20 kg/m^3 to larger values (Fig. 4e-f, and GROUP G in Supplementary Information 3), the possibilities of ponding types increase, whereas the possibilities of foundering firstly increase (Fig. 4e) and then decrease (Fig. 4f). This indicates that the density jump ≥20 kg/m^3 can lead to the lateral ponding or foundering of plume materials at ∼1000 km depth.

4. Discussion

4.1. Comparison of model predictions to observations

The broad penetration and necking types of plume behavior at the 1000 km discontinuity modeled here are comparable with tomographically detected broad penetration and necking of plume-related anomalies described in the introduction (Fig. 1), whereas aborted type likely accounts for unraised or slightly swelled slow anomalies near the core-mantle boundary (Durand et al., 2017; Ritsema et al., 2011).

There are so many hot spots and shallow low-velocity anomalies that almost all the laterally extending anomalies at ∼1000 km depth can be found to have a shallow counterpart above them. Although no clear conduits are detected between some laterally extending anomalies and shallow anomalies (French and Romanowicz, 2015), some researchers still suggest that they are all connected or were previously connected. If some of these laterally extending anomalies are truly connected or were connected to the shallow low-velocity anomalies, they may be examples of our foundering type (first penetration then ponding). Plume ponding is also demonstrated to be feasible at different depths by previous modeling studies (Dannberg and Sobolev, 2015; Samuel and Bercovici, 2006), in which some plumes may stagnate and abort without forming shallow counterparts (Dannberg and Sobolev, 2015; Samuel and Bercovici, 2006). Under this condition, the hot spot above may represent eruption of other adjacent plumes. Interestingly, synchronous and parallel upwelling of multiple deep plumes and their necking or broad penetration process can also form large-scale plume anomalies at ∼1000 km depth (e.g., Samoa, Tahiti and Marquesas in Fig. 1d) (French and Romanowicz, 2015). If the tomographic result is correct, this parallel upwelling of different plumes, likely has very complex initial conditions, and is not constrained in this work.

Our results are mostly comparable with seismically constrained tomographical models showing different plume behaviors at ∼1000 km depth (French and Romanowicz, 2015). However, other results, depending on different data or processing techniques, may not completely show such different behaviors of plumes at the same locations of these depths (Moulik and Ekström, 2014; Ritsema et al., 2011). Although comparison of different seismic studies have also confirmed a change in the global shear velocity pattern at ∼1000 km depth, corresponding to some untested changing of mantle properties (Durand et al., 2017), more comparative works should be carried out to confirm the detailed structures of each type of deep plume.

4.2. Viscosity stratification and plume necking at ∼1000 km depth

Čížková and Bina (2019) suggest that viscosity stratification can lead to slab deflection and stagnation at ∼1000 km depth. However, based on our model groups A and B (Fig. 4a, b), the viscosity stratification cannot lead to the lateral ponding of deep plumes at ∼1000 km depth. In fact, we find that a lower viscosity layer between 660-1000 km depths can accelerate the upwelling velocity of deep materials at ∼1000 km depth (Fig. 5). If the 660-1000 km depths are assumed to be as viscous as upper mantle materials (Čížková and Bina, 2019), when the hot plume rises to this low-viscosity layer, the upwelling velocity of the plume can become much faster due to reduced viscous stresses, whereas the buoyancy flux of the plume is maintained and is close to that of the model without viscosity stratification (Fig. 5), thus the conduit of the plume becomes significantly thinner above ∼1000 km depth (Fig. 5). It is similar when the hot plume enters the low-viscosity upper mantle from the high-viscosity lower mantle (Leng and Gurnis, 2012). We thus propose that the lower viscosity layer between 660-1000 km depths can only accelerate the upwelling of the plume to form plume necking above ∼1000 km depths (Fig. 5) rather than lateral ponding.

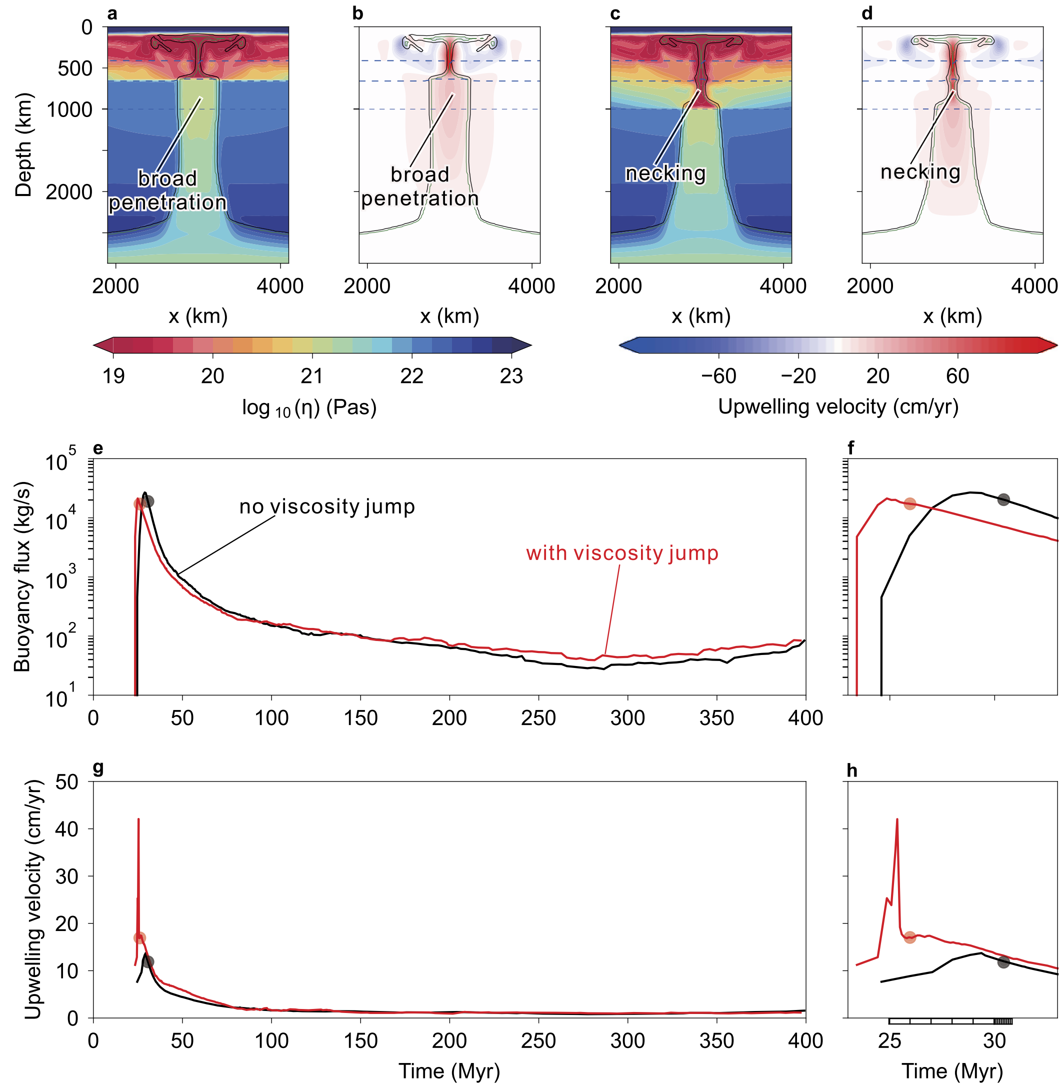

Fig. 5. Lower viscosity layer between 660-1000 km depths can accelerate upwelling to form necking. (a-b) No viscosity stratification at ∼1000 km depth. The snapshots in a and b are the viscosity field and upwelling velocity field of a model without viscosity stratification at ∼1000 km depth, in which ΔT=500 K, r=1000 km, initial volume= 0.76×10^9 km^3, $\Delta\rho_{1000} = 0$ and $\eta_{660-1000}$ is equivalent to η_{lower}. (c-d) With viscosity stratification at ∼1000 km depth. The snapshots in c and d are the viscosity field and upwelling velocity field of a model with the same parameters (ΔT=500 K, r=1000 km, initial volume= 0.76×10^9 km^3, $\Delta\rho_{1000} = 0$) as those used in a and b, but without viscosity stratification at ∼1000 km depth ($\eta_{660-1000} = \eta_{upper}$). (e) Plume buoyancy flux evolution at ∼1000 km depth in a (dark line) and c (red line), red and dark points indicate the time for snapshots a, b and c, d, respectively. (f) zoom-in of e between 23-33 Myr. (g) Plume average upwelling velocity evolution between 660-1000 km depths (taking the region with an excess temperature higher than 25 K for average) in a (dark line) and c (red line). (h) zoom-in of g between 23-33 Myr.

4.3. Compositional density stratification and plume ponding at ∼1000 km depth

Plume ponding or stagnation has been demonstrated as a result of upwelling of Si-enriched source materials (Samuel and Bercovici, 2006). This can lead to a significant increase in the compositional density contrast with decreasing pressure and make plumes stagnate at a depth of neutral buoyancy in the lower mantle. This can explain plume stagnation at different lower-mantle depths, but has difficulties to explain the multiple behaviors and relative concentrations of plumes extending specifically at 1000 km (French and Romanowicz, 2015). Actually, the buoyancy of plumes is not only influenced by plume properties, but also influenced by the surrounding mantle properties. Many studies thus suggest, aside from the intrinsic features of plume source materials, the ambient mantle at ∼1000 km depth likely plays a more important role (Čížková and Matyska, 2004).

Ballmer et al. (2015) have shown that a composition-induced density jump at ∼1000 km depth can lead to stagnation of subducting slabs near this depth. According to our results, a sufficient compositional density contrast (15-20 kg/m^3) rather than viscosity change near 1000 km depth is conducive to lateral ponding of deep plumes at ∼1000 km depth (Fig. 3b, e and Fig. 4e, f). This density contrast value is close to those threshold values (12-15 kg/m^3) revealed in previous studies for regional double-layered convection or regional slab stagnation (Ballmer et al., 2015; Yan et al., 2020). A density stratification scheme is consistent with the speculations of Durand et al. (2017) and Waszek et al. (2018) that the compositional density stratification has an effect on deep plumes at ∼1000 km depth. Combining the multiple types of plume behavior at ∼1000 km depth, it is reasonable to propose that the density structure at ∼1000 km depth in the Earth's mantle is not homogenous, but with some regions having radial contrast ≥20 kg/m^3 and other regions having lower density contrast ≤15 kg/m^3 or a more gradual boundary. Thus, some deep plumes pond at ∼1000 km depth, and some others pass through this depth with broad conduits. This laterally heterogeneous density stratification idea is consistent with results from previous modeling works based on a whole-mantle convection system, in which regional slab stagnation is stable in well-stratified regions and not stable in less-stratified regions (Ballmer et al., 2017; Gülcher et al., 2020a).

Additionally, this laterally heterogeneous density stratification scheme does not contradict or invalidate the viscosity stratification idea. In contrast, they can coexist, although our modeling shows that the viscosity stratification is not the decisive factor for plume ponding, but rather, it is the decisive factor for plume necking. Considering the geophysically detected necking of some deep plumes at ∼1000 km depth, we suggest that large-scale significant viscosity heterogeneities may coexist or may even be coupled with density heterogeneities in some regions at ∼1000 km depth in the Earth's mantle.

4.4. The possible genesis of ∼1000 km depth compositional density stratification

Building on the research, model results and speculations of Durand et al. (2017) and Waszek et al. (2018), we suggest that the lateral ponding of deep plumes near 1000 km depth depends on the regional compositional density stratification in the lower mantle, whereas the necking depends on the regional viscosity stratification. The possible origins of regional viscosity stratification at ∼1000 km depth include compositional variation, regional variations in dehydration and hydration, pressure induced viscosity changes in ferropericlase and bridgmanite, grain-size related viscosity changes, and gradual transformation between garnet-majorite solid solution and bridgmanite, as discussed in previous works (Čížková and Bina, 2019; Rudolph et al., 2015).

The origin of the compositional density stratification at ∼1000 km depth might be the boundary between the depleted mantle and primordial mantle domains. Throughout Earth's history, multiple partial melting episodes have taken place in the shallow mantle to form the oceanic crust and depleted mantle (Lee, 2003; Vervoort and Blichert-Toft, 1999), whereas the deep mantle underwent fewer partial melting episodes and preserves more primordial materials (bridgmanite-enriched?), as introduced by previous works (Ballmer et al., 2017; Gülcher et al., 2020a,b). The density of the depleted mantle is relatively lower than the primordial materials (Ballmer et al., 2017; Lee, 2003; Schutt and Lesher, 2006). The density contrast is a function of Mg# or function of Mg/Si ratio, and can be between 0-92.43 kg/m^3 (Gülcher et al., 2020b) or 0-65 kg/m^3 (Ballmer et al., 2017) or less according to previous works (Lee, 2003), and is comparable with the value range investigated in our models in GROUP E-F (≥20 kg/m^3) to GROUP G (100 kg/m^3 in Supplementary Information 3). Such compositional density stratification, according to our research, can lead to deep plumes laterally ponding at this boundary, or result in them first penetrating the boundary and then foundering to ∼1000 km depth or deeper. The ponding or final foundering of compositionally dense materials entrained by the hot plume can reduce the material loss of the primordial layer and is conducive to its long-term preservation.

Waszek et al. (2018) suggest that there has been a large-scale heterogeneous geochemical reservoir in the mid-mantle for a long time. Ballmer et al. (2017), Nakagawa et al. (2010), and Gülcher et al. (2020a,b) demonstrate that large amounts of primordial materials can survive and be sustained as regional, large-scale, compositionally dense blobs in the lower mantle after billions of years of whole-mantle convection. This idea is quite similar to the one proposed here that a density jump with different magnitude contrast degrees is distributed at ∼1000 km depth. However, the plumes in those models rise mostly from depleted domains (high Mg/Si) and surround the primordial bobs (Ballmer et al., 2017), whereas plumes in our models are dominated by compositionally dense materials at the core-mantle boundary and can rise through or within the primordial bobs. In fact, the "surround effect" in previous studies (Ballmer et al., 2017) is usually overemphasized in 2D models. In a more realistic 3D model, the primordial blobs are not surrounded by plumes with elliptic horizontal sections (Zhong, 2006), instead, they are deformed and passed through by plume materials. This point more resembles the ones modeled by Čížková and Matyska (2004), in which high-density materials are passed through by plumes and slabs, and can also be stable in the lower mantle after billions of years of whole-mantle convection. However, in these models, the early mantle is supposed to be already layered at their initial setups, whereas the conditions in the early Earth were likely much more complex (e.g., Korenaga, 2021; Sleep, 1990). The formation and long-time evolution or preservation of a layered mantle structure, and their relative roles in the Earth's evolution, are still opening directions.

If the ponding of low-velocity anomalies at ∼ 1000 km depth are valid, the density stratification scheme is the best mechanism according to this work. This density jump is generally at ∼1000 km depth, but regionally deeper or shallower in some places (Anderson, 2006; Kellogg et al., 1999). The depth variation for this jump likely indicates moderate stratification of the Earth's mantle (Kellogg et al., 1999), via long time partial melting, differentiation and stirring effects of subduction and plume activities (Ballmer et al., 2017; Čížková and Matyska, 2004).

According to our modeling results and variation of plume-related geophysical anomalies, we propose a model for the incomplete stratification of Earth's mantle at ∼1000 km depth (Fig. 6). This stratification includes radial viscosity and density changes with different lateral scales and magnitude levels at ∼1000 km depth. In places where depleted mantle has the lowermost boundary at ∼1000 km depth, the density contrast is likely large (≥20 kg/m^3), and plume ponding and foundering may be generated. In places where the stratification is gradual or the lowermost boundary is much shallower than ∼1000 km depth, the density contrast is likely small (≤15 kg/m^3) at ∼1000 km, thus broad plume penetration can be formed. In places where the viscosity at 660-1000 km depths is low, plume necking can be formed (Fig. 6). Therefore, this moderate stratification can explain the different behavior of plume at ∼ 1000 km depth.

4.5. Model limitation

Our results are limited in 2D geometry, whereas plumes passing though deep mantle domains can be more sufficiently reflected in 3D global spherical models (e.g., Zhong, 2006). In our models, the plate motion or mantle flow are initially driven by deep upwelling, and no specific plate velocity and mantle flow are adopted within a plate tectonic paradigm, thus no obvious lateral shifting of plume trails is produced in most of our models. For the real Earth, lateral mantle flow (or mantle wind) or shallow plate motions (e.g., Steinberger and Antretter, 2006; Tarduno et al., 2009) are essential for the lateral shifting of plume conduits (French and Romanowicz, 2015). Besides, viscosity induced mantle flow pattern changes at ∼1000 km depth (viscosity jump/gradient) may also lead to lateral displacements of plumes near this boundary (e.g., Rudolph et al., 2015).

The viscosity stratification at ∼660 km and ∼1000 km depths (Čížková and Bina, 2019) adopted here are also used in other modeling works (e.g., Čížková and Bina, 2019; Gülcher et al., 2020a,b; Leng and Gurnis, 2012). However, an additional viscosity jump at ∼410 km depth suggested and adopted in other modeling works is not used in this work. If present, this boundary can also cause the plume to neck or pond at the 410 km phase boundary (Ballmer et al., 2013; Dannberg and Sobolev, 2015) rather than neck at ∼1000 or 660 km as in this work. Viscosity and density boundaries may be complexly coupled with each other in some places (Ballmer et al., 2017), however the models here are relatively simple and only

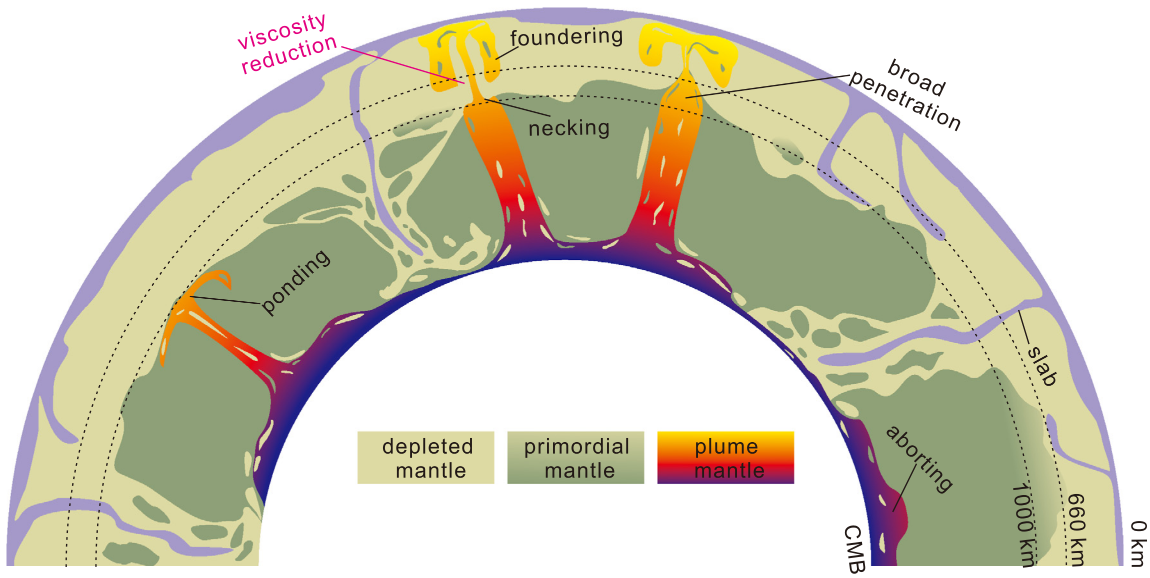

Fig. 6. Sketch of large-scale regional stratification of Earth's mantle and different deep plume behaviors at ∼1000 km depth in a whole-mantle convection system, with involvement of depleted and primordial mantle domains.

investigate pure viscosity stratification or pure density stratification.

Plume theories, especially the ones supporting plumes with lower-mantle origin are not universally accepted because of large uncertainties and complexities in geophysical observations and interpretations (Anderson, 2000; Maguire et al., 2016). Thus, the limitations and accuracy of these models should be tested and discussed in future works.

5. Conclusion

Through numerical modeling, we tested the broad penetration, necking, lateral ponding, foundering and aborting of different plumes influenced by viscosity and density boundaries at ∼1000 km depth in the Earth's mantle to investigate the controlling factors of different slow-velocity anomalies near this depth. We find that the viscosity stratification can only lead to plume necking, whereas different level of density changes can explain broad penetration, ponding and foundering. We thus suggest that a compositional boundary probably exists incompletely at ∼1000 km depth in the mantle, and speculate that it is probably the boundary between the depleted and primordial domains, that has been progressively evolving during the stratification of the Earth's mantle through melt extraction and mantle stirring throughout history.

CRediT authorship contribution statement

Zhensheng Wang designed research; Guanjie Xiang and Zhensheng Wang performed research, analyzed data, and performed data interpretation; all co-authors wrote the paper.

Declaration of competing interest

The authors declare that they have no known competing financial interests or personal relationships that could have appeared to influence the work reported in this paper.

Acknowledgements

The two anonymous reviewers and Professor James Badro are thanked for their constructive comments, which greatly improve this study. This study was supported by the grants National Natural Science Foundation of China (grants 41802217, 41572203, 91755213 and 40821061), the Fundamental Research Funds for the Central Universities, China University of Geosciences (Wuhan) (grant CUG 180621) and MOST Special Fund from the State Key Laboratory of GPMR (grants MSFGPMR20, MSFGPMR02-3). The calculation/modeling work in this article used the Goody-1 HPC of School of Earth Science at the China University of Geosciences.

Data and tomographic model in Fig. 1 can be obtained at the website (https://www.earth.ox.ac.uk/~smachine/cgi/index.php). All numerical modeling data in Fig. 2–5 are calculated using underworld2 (https://doi.org/10.5281/zenodo.3384283).

Appendix A. Supplementary material

Supplementary material related to this article can be found online at https://doi.org/10.1016/j.epsl.2021.117213.

References

Anderson, D.L., 2000. The thermal state of the upper mantle; no role for mantle plumes. Geophys. Res. Lett. 27 (22), 3623–3626.
Anderson, D.L., 2006. Speculations on the nature and cause of mantle heterogeneity. Tectonophysics 416 (1), 7–22.
Ballmer, M.D., Houser, C., Hernlund, J.W., Wentzcovitch, R.M., Hirose, K., 2017. Persistence of strong silica-enriched domains in the Earth's lower mantle. Nat. Geosci. 10 (3), 236–240.
Ballmer, M.D., Ito, G., Wolfe, C.J., Solomon, S.C., 2013. Double layering of a thermochemical plume in the upper mantle beneath Hawaii. Earth Planet. Sci. Lett. 376, 155–164.
Ballmer, M.D., Schmerr, N.C., Nakagawa, T., Ritsema, J., 2015. Compositional mantle layering revealed by slab stagnation at ∼1000-km depth. Sci. Adv. 1 (11), e1500815.
Bullen, K.E., 1940. The problem of the Earth's density variation. Bull. Seismol. Soc. Am. 30, 235–250.
Bullen, K.E., 1947. Introduction to the Theory of Seismology.
Čížková, H., Bina, C.R., 2019. Linked influences on slab stagnation: interplay between lower mantle viscosity structure, phase transitions, and plate coupling. Earth Planet. Sci. Lett. 509, 88–99.
Čížková, H., Matyska, C., 2004. Layered convection with an interface at a depth of 1000 km: stability and generation of slab-like downwellings. Phys. Earth Planet. Inter. 141 (4), 269–279.
Čížková, H., van den Berg, A.P., Spakman, W., Matyska, C., 2012. The viscosity of Earth's lower mantle inferred from sinking speed of subducted lithosphere. Phys. Earth Planet. Inter. 200–201, 56–62.
Dannberg, J., Sobolev, S.V., 2015. Low-buoyancy thermochemical plumes resolve controversy of classical mantle plume concept. Nat. Commun. 6, 6960.

Davaille, A., 1999. Two-layer thermal convection in miscible viscous fluids. J. Fluid Mech. 379, 223–253.

Durand, S., Debayle, E., Ricard, Y., Zaroli, C., Lambotte, S., 2017. Confirmation of a change in the global shear velocity pattern at around 1000 km depth. Geophys. J. Int. 211 (3), 1628–1639.

Farnetani, C.G., 1997. Excess temperature of mantle plumes: the role of chemical stratification across D". Geophys. Res. Lett. 24 (13), 1583–1586.

French, S.W., Romanowicz, B., 2015. Broad plumes rooted at the base of the Earth's mantle beneath major hotspots. Nature 525 (7567), 95–99.

Fukao, Y., Obayashi, M., 2013. Subducted slabs stagnant above, penetrating through, and trapped below the 660 km discontinuity. J. Geophys. Res., Solid Earth 118 (11), 5920–5938.

Gülcher, A.J.P., Ballmer, M.D., Tackley, P.J., 2020a. Coupled dynamics and evolution of primordial and recycled heterogeneity in Earth's lower mantle. Solid Earth Discuss. 2020, 1–43.

Gülcher, A.J.P., Gebhardt, D.J., Ballmer, M.D., Tackley, P.J., 2020b. Variable dynamic styles of primordial heterogeneity preservation in the Earth's lower mantle. Earth Planet. Sci. Lett. 536, 116160.

Hansen, U., Yuen, D.A., 1988. Numerical simulations of thermal-chemical instabilities at the core-mantle boundary. Nature 334 (6179), 237–240.

Hoggard, M.J., Parnell-Turner, R., White, N., 2020. Hotspots and mantle plumes revisited: towards reconciling the mantle heat transfer discrepancy. Earth Planet. Sci. Lett. 542, 116317.

Ito, E., Takahashi, E., 1989. Postspinel transformations in the system Mg_2SiO_4-Fe_2SiO_4 and some geophysical implications. J. Geophys. Res., Solid Earth 94 (B8), 10637–10646.

Katsura, T., Yoneda, A., Yamazaki, D., Yoshino, T., Ito, E., 2010. Adiabatic temperature profile in the mantle. Phys. Earth Planet. Inter. 183 (1–2), 212–218.

Kellogg, L.H., Hager, B.H., van der Hilst, R.D., 1999. Compositional stratification in the deep mantle. Science 283 (5409), 1881–1884.

Korenaga, J., 2021. Hadean geodynamics and the nature of early continental crust. Precambrian Res. 359, 106178.

Lee, C.A., 2003. Compositional variation of density and seismic velocities in natural peridotites at STP conditions: implications for seismic imaging of compositional heterogeneities in the upper mantle. J. Geophys. Res., Solid Earth 108 (B9).

Leng, W., Gurnis, M., 2012. Shape of thermal plumes in a compressible mantle with depth-dependent viscosity. Geophys. Res. Lett. 39 (5).

Maguire, R., Ritsema, J., van Keken, P.E., Fichtner, A., Goes, S., 2016. P- and S-wave delays caused by thermal plumes. Geophys. J. Int. 206 (2), 1169–1178.

Moresi, L., Dufour, F., Mühlhaus, H.B., 2003. A Lagrangian integration point finite element method for large deformation modeling of viscoelastic geomaterials. J. Comput. Phys. 184 (2), 476–497.

Moulik, P., Ekström, G., 2014. An anisotropic shear velocity model of the Earth's mantle using normal modes, body waves, surface waves and long-period waveforms. Geophys. J. Int. 199 (3), 1713–1738.

Nakagawa, T., Tackley, P.J., Deschamps, F., Connolly, J.A.D., 2010. The influence of MORB and harzburgite composition on thermo-chemical mantle convection in a 3-D spherical shell with self-consistently calculated mineral physics. Earth Planet. Sci. Lett. 296 (3), 403–412.

Ringwood, A.E., 1970. Phase transformations and the constitution of the mantle. Phys. Earth Planet. Inter. 3, 109–155.

Ritsema, J., Deuss, A., van Heijst, H.J., Woodhouse, J.H., 2011. S40RTS: a degree-40 shear-velocity model for the mantle from new Rayleigh wave dispersion, teleseismic traveltime and normal-mode splitting function measurements. Geophys. J. Int. 184 (3), 1223–1236.

Rudolph, M.L., Vedran, L., Lithgow-Bertelloni, C., 2015. Viscosity jump in Earth's mid-mantle. Science 350 (6266), 1349.

Samuel, H., Bercovici, D., 2006. Oscillating and stagnating plumes in the Earth's lower mantle. Earth Planet. Sci. Lett. 248 (1), 90–105.

Schutt, D.L., Lesher, C.E., 2006. Effects of melt depletion on the density and seismic velocity of garnet and spinel lherzolite. J. Geophys. Res., Solid Earth 111 (B5).

Sleep, N.H., 1990. Hotspots and mantle plumes: some phenomenology. J. Geophys. Res., Solid Earth 95 (B5), 6715–6736.

Sobolev, S.V., et al., 2011. Linking mantle plumes, large igneous provinces and environmental catastrophes. Nature 477 (7364), 312–316.

Steinberger, B., Antretter, M., 2006. Conduit diameter and buoyant rising speed of mantle plumes: implications for the motion of hot spots and shape of plume conduits. Geochem. Geophys. Geosyst. 7 (11).

Tarduno, J., Bunge, H., Sleep, N., Hansen, U., 2009. The bent Hawaiian-emperor hotspot track: inheriting the mantle wind. Science 324 (5923), 50–53.

Tosi, N., Yuen, D.A., De Koker, N., Wentzcovitch, R.M., 2013. Mantle dynamics with pressure- and temperature-dependent thermal expansivity and conductivity. Phys. Earth Planet. Inter. 217 (Complete), 48–58.

van den Berg, A.P., van Keken, P.E., Yuen, D.A., 1993. The effects of a composite non-Newtonian and Newtonian rheology on mantle convection. Geophys. J. Int. 115 (1), 62–78.

van Hunen, J., van den Berg, A.P., Vlaar, N.J., 2002. On the role of subducting oceanic plateaus in the development of shallow flat subduction. Tectonophysics 352 (3), 317–333.

Vervoort, J.D., Blichert-Toft, J., 1999. Evolution of the depleted mantle: Hf isotope evidence from juvenile rocks through time. Geochim. Cosmochim. Acta 63 (3), 533–556.

Waszek, L., Schmerr, N., Ballmer, M., 2018. Global observations of reflectors in the mid-mantle with implications for mantle structure and dynamics. Nat. Commun. 9.

Wood, B.J., 1990. Postspinel transformations and the width of the 670-km discontinuity: a comment on "postspinel transformations in the system Mg_2SiO_4–Fe_2SiO_4 and some geophysical implications" by E. Ito and E. Takahashi. J. Geophys. Res., Solid Earth 95 (B8), 12681–12685.

Xu, W., Lithgow-Bertelloni, C., Stixrude, L., Ritsema, J., 2008. The effect of bulk composition and temperature on mantle seismic structure. Earth Planet. Sci. Lett. 275 (1), 70–79.

Yan, J., Ballmer, M.D., Tackley, P.J., 2020. The evolution and distribution of recycled oceanic crust in the Earth's mantle: insight from geodynamic models. Earth Planet. Sci. Lett. 537, 116171.

Zhong, S., 2006. Constraints on thermochemical convection of the mantle from plume heat flux, plume excess temperature, and upper mantle temperature. J. Geophys. Res., Solid Earth 111 (B4).